Available online at www.sciencedirect.com
SCIENCE DIRECT®
Dynamics of Atmospheres and Oceans
40 (2005) 43–56
dynamics of atmospheres and oceans
www.elsevier.com/locate/dynatmoce

Numerical and laboratory generation of internal waves from turbulence

K. Dohan*, B.R. Sutherland

Department of Mathematical and Statistical Sciences, University of Alberta, Edmonton, Alta., Canada T6G 2G1

Received 16 December 2003; accepted 4 October 2004
Available online 3 February 2005

Abstract

Numerical simulations of internal waves that are generated from eddies within a mixed region are described and are directly compared to laboratory observations. The mixed region is created in the laboratory by an oscillating grid at the top of a uniformly salt-stratified region. A tank with a length-to-width ratio of 5:1 is used in order to visualize the internal waves and, as such, large-scale waves are produced from a mean circulation which develops in the mixed region. In addition, smaller-scale waves are generated from the turbulent eddies. Fully non-linear numerical simulations in two dimensions of a mixed region overlying a uniformly stratified region are performed to investigate separately the large-scale and small-scale generation of waves from a mixed region, and the qualitative results compare well with the experimental results. This suggests that the first order dynamics of the laboratory experiments may be captured by the simulations of the two-dimensional model.

Keywords: Internal gravity wave; Turbulence; Laboratory experiment; Numerical simulation

1. Introduction

The Earth's climate is significantly influenced by the meridional transport of heat by the general circulations of both the atmosphere and oceans. It is currently believed that

* Corresponding author. Present address: Scripps Institution of Oceanography, University of California, San Diego, 9500 Gilman Drive MC 0230, La Jolla, CA 92093-0230, USA. Tel.: +858 822 4325; fax: +858 534 9820.
E-mail address: kdohan@ucsd.edu (K. Dohan).

0377-0265/$ – see front matter © 2004 Elsevier B.V. All rights reserved.
doi:10.1016/j.dynatmoce.2004.10.004

the ocean is responsible for 8% of the transport of heat in the southern hemisphere and 22% in the northern hemisphere (Trenberth and Caron, 2001). The vertical mixing of heat across density surfaces in the ocean is a vital step in ocean circulation. Determining the vertical mixing rate is difficult because ocean models cannot resolve the scales of turbulent motions and although ocean turbulent dissipation rates have been measured for numerous years, it is impractical to measure the turbulent dissipation rates at all locations throughout the oceans. An understanding of the mechanisms of turbulent mixing is necessary in order to parameterize the small-scale processes for use in large-scale ocean models.

Until recently, it was assumed out of simplicity that diapycnal mixing occurred uniformly throughout the ocean interior. A clear contradiction of this assumption was revealed by observations of enhanced mixing in the deep ocean during the Mid-Atlantic Ridge Tracer Release Experiment, (Polzin et al., 1997; Ledwell et al., 2000) in which large turbulent dissipation rates were found over the rough, steep slopes of the ridge. Egbert and Ray (2000) used satellite altimetry data to estimate the dissipation of barotropic tidal energy throughout the oceans and showed that between 25% and 30% of the total tidal dissipation takes place in the deep ocean, generally near areas of rough topography. St.Laurent and Garrett (2002) calculate that almost all of the power in the barotropic tide is converted to internal tides, which eventually dissipate, thereby mixing the deep ocean.

The emphasis on the properties of the observed wave field generated by flow over bottom topography vary with the observation time, as depicted in the schematic of Fig. 1. Over very long times relative to the inertial period ($t_{\text{obs}} \gg T_{\text{inertial}}$, where $T_{\text{inertial}} \equiv 2\pi/f$ and f is the Coriolis frequency) the long-term properties of the internal tides can be observed. Over intermediate times, on the order of a day, the tidal flow can be viewed as uniform flow over topography. On very fast time-scales, such as hours or minutes, the details of the small-scale processes such as turbulence generated by flow over rough topography can be observed.

Much attention has been devoted to the investigation of the conversion of power from the barotropic tide to internal (baroclinic) tides by both supercritical and subcritical topog-

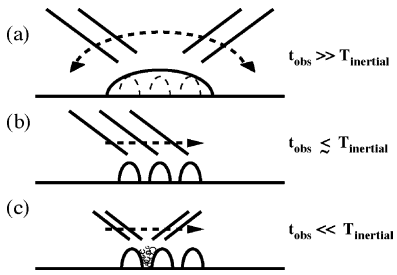

Fig. 1. Different time-scales for observations of wave fields. (a) Time-scales of observations longer than the inertial period result in measurements of average statistics of internal tides. (b) On time-scales on the order of the inertial period, the motion of the tides can be locally viewed as uniform flow over topography, with internal waves viewed as lee waves. (c) On very short observation time-scales, the small-scale generation mechanisms can be considered.

raphy (e.g. recently by Llewellyn Smith and Young (2002), Balmforth et al. (2002) and St.Laurent and Garrett (2002)). Here, we discuss the possibility of the third generation situation depicted in Fig. 1c, in which non-hydrostatic internal waves are generated from the turbulent eddies.

Another potentially important source for turbulence-generated waves in the ocean is the surface mixed layer. Munk and Wunsch (1998) estimated that wind-generated internal waves may provide half of the energy needed for mixing the ocean interior. Although inertial waves created by large motions such as severe storms are likely the main source of energy, the role that the small-scale internal gravity waves play is unknown.

We have used oscillating grid experiments in the laboratory to study the wave field in a uniformly stratified region generated from a turbulent layer (Dohan and Sutherland, 2003). The emphasis of the majority of past oscillating-grid studies has been on the properties of the turbulent region, such as examining the entrainment rate (Linden, 1975; E and Hopfinger, 1986). There have been some theoretical (Fernando and Hunt, 1997), experimental (McGrath et al., 1997) and numerical (Briggs et al., 1996) studies to examine the internal waves, although the waves were on the interface between the turbulent region and the approximately quiescent region below.

The emphasis of our studies has been on the vertically propagating wave field within the quiescent region, rather than on the turbulence or interfacial waves. We have been using numerical simulations to simulate a mixed layer overlying a stratified region in order to examine further the generation of internal waves from a mixed region. Although we generate downward-propagating waves from the base of a turbulent mixed region, we are in the parameter regime in which the Boussinesq approximation is applicable and the results are also applicable to upward-propagating waves such as described above. In this paper, we qualitatively compare the wave field generated in the laboratory experiments with the numerical simulations as a step to understanding the general properties of turbulence-generated waves. We demonstrate that the features and trends of the laboratory wave field are reproduced in the two-dimensional numerical model.

2. Set-up

2.1. Laboratory experiments

A series of oscillating grid experiments in a salt–water tank were performed in order to examine the properties of the internal wave field generated from the turbulence in a mixed region.

An oscillating grid was used to create a mixed region at the top of a tank filled with uniformly stratified salt water. The tank was a transparent perspex tank with dimensions $L = 47.6$ cm, $W = 9.7$ cm and $H = 49$ cm. The narrow width of tank, relative to the length, was necessary in order to create an approximately two-dimensional wave field, which could be viewed through the long side of the tank.

The metal grid of 0.6 cm bars spaced 3.2 cm apart, spanned the full horizontal cross-section of the tank and was placed 5 cm below the free surface of the water. The frequency of oscillation was fixed at 7 Hz, with a peak-to-peak stroke length of 2.6 cm.

The strength of the stratification is typified by the squared buoyancy frequency, $N^2 = -\frac{g}{\rho_0}\frac{\mathrm{d}\overline{\rho}}{\mathrm{d}z}$, where $\overline{\rho}(z)$ is the background density profile, ρ_0 is a reference density (1.0 g/cm^3) and g is the gravitational acceleration. The uniform stratification was varied between experiments with constant values of N^2 ranging between 0.11 s^{-2} and 1.96 s^{-2}. The corresponding buoyancy periods, $T_{\mathrm{buoy}} = 2\pi/N$, were orders of magnitude larger than the stroke period of the oscillating grid.

Both dye lines and synthetic schlieren (Sutherland et al., 1999) were used to visualize the wave field. Dye lines marked the motions of isopycnal layers at three vertical positions, while the schlieren technique indirectly measured the entire wave field, without the use of dyes.

The experimental set-up and measurement techniques are described in more detail in Dohan and Sutherland (2002, 2003).

2.2. Numerical model

The generation of internal waves from a mixed region is further examined by numerically simulating a uniformly stratified Boussinesq fluid underlying a homogeneous mixed region. The model solves the fully non-linear, non-hydrostatic, Navier-Stokes and mass conservation equations in two dimensions. A two-dimensional model is used both for the simplest first comparison with the laboratory experiments and to decrease computational time enough to allow for multiple simulations.

The equations for the basic-state fields of vorticity, ζ, and perturbation density, ρ, in dimensional units are:

$$u_x + w_z = 0 \tag{1}$$

$$\frac{\mathrm{D}\zeta}{\mathrm{D}t} = \frac{g}{\rho_0}\frac{\partial\rho}{\partial x} + \nu\nabla^2\zeta + F_\zeta \tag{2}$$

$$\frac{\mathrm{D}\rho}{\mathrm{D}t} + w\frac{\mathrm{d}\overline{\rho}}{\mathrm{d}z} = \kappa\nabla^2\rho \tag{3}$$

where subscripts denote partial derivatives, $\mathrm{D}/\mathrm{D}t = \partial/\partial t + \mathbf{u}\cdot\nabla$, ρ_0 is the density at a reference level, ν the kinematic viscosity, κ the mass diffusivity, and the pressure and density are expressed in terms of their background and perturbation values:

$$\rho_{\mathrm{total}} = \overline{\rho}(z) + \rho(x, z, t) \tag{4}$$

$$p_{\mathrm{total}} = \overline{p}(z) + p(x, z, t) \tag{5}$$

$$\frac{\mathrm{d}\overline{p}}{\mathrm{d}z} = -\overline{\rho}g. \tag{6}$$

The vorticity field is forced with the term F_ζ, described in the sections below.

The streamfunction is related to the horizontal and vertical velocity components by $(u, w) = (-\psi_z, \psi_x)$, so that the velocities can be determined from the vorticity by inverting the elliptic equation:

$$\nabla^2\psi = -\zeta. \tag{7}$$

Eqs. (2) and (3) are evolved using second order finite difference in the vertical, Fourier spectral method in the horizontal and stepped forward in time using a leapfrog method with an Euler backstep every 20 time intervals to minimize splitting errors. The details of the numerical model are given in Sutherland and Peltier (1994).

The domain is a horizontally periodic channel with free-slip upper and lower boundary conditions. In the simulations reported upon here the domain extends from $-20 \leq x \leq 20$ cm, and $0 \leq z \leq 80$ cm with a resolution of 512×1024 points and $\Delta t = 0.002$ s. The domain is set to be of comparable width to the laboratory experiments, but approximately twice as deep, in order to delay bottom reflection and to ensure observations of the downward-propagating waves alone. The domain size is chosen as a compromise between extending the wave region and computation time. For example, a simulation requires approximately 1 h using 16 CPUs on the WestGrid supercomputer cluster (http://www.westgrid.ca) to run 1 s of the simulation. Simulations are run typically for 60 s, requiring a total of 1000 CPU hours.

The mixed layer is simulated by a homogeneous top layer that overlies a uniformly stratified region. The initial stratification is given by:

$$N = \begin{cases} N_0^2 & 0 \leq z < 60 \\ 0 & 60 \leq z \leq 80. \end{cases}$$

The simulations are run with values of $N_0^2 = 1\,\mathrm{s}^{-2}$, $\nu = 0.01\,\mathrm{cm}^2/\mathrm{s}$, and $\mathrm{Pr} = \nu/\kappa = 1$. The kinematic viscosity was chosen to be that of water, but the unphysically high value for the mass diffusivity was chosen in order to damp out small-scale numerical noise for numerical stability. The vorticity field in the mixed region is continuously forced by the term $F_\zeta(x, z, t)$ in Eq. (2). We describe two types of simulations in which the mixed region is forced first with a large circulation in Section 3.1 and second with random vorticity at high wavenumbers in Section 3.2.

3. Observations

3.1. Large-scale waves

The tank was initially stratified throughout its depth. The experiments began by switching on the oscillating grid. The majority of the mixed layer depth was established within the first 5 s and slowly deepened (on the order of 5 cm) throughout the duration of the experiments. The observations were made within the first few minutes of an experiment, well before the onset of non-linear interactions between downward-propagating waves and reflected waves.

Due to the large horizontal aspect ratio of the tank, turbulent motions larger than the width of the tank were constrained to the vertical plane and two counter-rotating vortices consistently developed in the mixed region. The vortices filled the mixed region and had the form shown in the schematic Fig. 2a, with flow up the short sides of the tank. These continuously excited waves on the scale of the tank. Along with the tank-scale waves,

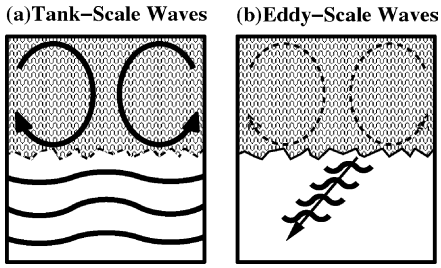

Fig. 2. Schematic views through the long side of the tank depicting the two scales of internal waves. (a) A mean circulation in the mixed region excited tank-scale internal waves. Dye lines marking isopycnal layers highlighted these large-scale motions. (b) Smaller-scale downward-propagating internal waves were generated on the scale of the smaller eddies and jets in the turbulence.

smaller-scale downward-propagating waves were also continuously generated from the eddies and jets in the turbulence, as depicted in Fig. 2b.

A view through the front of the tank in a dye-line experiment for which $N = 0.79\,\mathrm{s}^{-1}$ is shown in Fig. 3a at time $t = 2.4T_{\mathrm{buoy}}$. The turbulent region at the top is highlighted by pearlescence (Mearlmaid Natural Pearl Essence AA) and the oscillating grid can be seen near the top of the turbulent region. A fluorescent dye was used to mark three isopycnal layers, which were lit from the right of the tank. The tank-scale waves are the dominant waves visualized by the dye lines. These waves have an overall mode 2 in the horizontal structure, with nodes at $x = L/4, 3L/4$.

Motivated by the circulations in the laboratory experiments described above, numerical simulations are performed in which two counter-rotating vortices are forced in the mixed

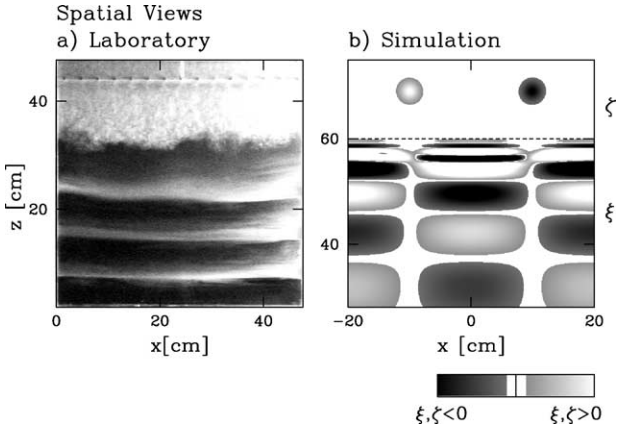

Fig. 3. (a) View through the front (long side) of a laboratory experiment. Three dye lines mark the vertical motions of isopycnal layers and are illuminated from the right. The turbulent region extends from $z = 47$ cm to $z \approx 27$ cm. (b) Vertical displacement field, ξ, and superimposed vorticity field, ζ, for a numerical simulation showing the same field of view as in (a). The large-scale wave field structure is mode 2 in the horizontal.

region:

$$F_\zeta = F_0 \exp\left[-\frac{1}{2}\left(\frac{(x+10)^2+(z-70)^2}{\sigma^2}\right)\right] - F_0 \exp\left[-\frac{1}{2}\left(\frac{(x-10)^2+(z-70)^2}{\sigma^2}\right)\right]. \quad (8)$$

In this simulation, the forcing amplitude is $F_0 = 0.1\,\mathrm{s}^{-2}$, the width of the Gaussian vortices is $\sigma = 2.0\,\mathrm{cm}$, and the forcing to the vorticity is added at every time step. The spatial structure of the generated internal waves is independent of the magnitude of F_0 and σ. The vortices are symmetrically placed within the mixed region and the aspect ratio of the mixed region is 1:1. Otherwise, the horizontal balance of vorticity is broken and a mean flow develops in the mixed region.

A sample perturbation density field is shown in Fig. 3b, for the same field of view as the experiment, although the bottom of the simulation extends beyond the window to $z = 0\,\mathrm{cm}$. The density field is scaled to correspond with vertical displacement for linear waves. The mixed region in this simulation spans $60 < x < 80\,\mathrm{cm}$, and the vortices are symmetrically placed in the centre of this region. The vorticity field is superimposed on the figure to show the structure of the vortices. Below the mixed region, waves are generated by the motion of the vortices and have the same mode 2 in the horizontal structure as observed in the experiments.

In the analysis of the laboratory experiments, the spectrum of frequencies present in the vertical motions of the isopycnal layers were complicated, with several peaks in the spectrum that did not correspond to the simplest vertical modes of the tank. The advantage to the simulations is that the evolution of the large-scale wave field can be seen throughout the stratified region, as opposed to the laboratory observations which were limited to three isopycnal layers.

The figure shows the dispersive nature of the waves, and explains the experimental results: the vertical wavelengths vary with distance from the mixed region, and there is no modal structure in the vertical. The largest vertical wavelengths in the figure are comparable to the depth of the laboratory domain. The extended vertical domain in the simulations is necessary in order to understand the vertical structure to the wave field prior to bottom reflection.

As well, qualitatively, the simulations are exhibiting the same trend in decreasing wave amplitudes with increasing stratification as measured in the experiments.

3.2. Small-scale waves

The mean circulations in the laboratory experiments generated tank-scale waves. In addition to these waves, smaller-scale downward-propagating waves were generated from the turbulent jets and eddies. The dominant waves were on a smaller scale than the modal waves described above, but on a larger scale than the smallest eddies in the turbulence.

A sample experimental wave field is shown in Fig. 4a. In this experiment, $N = 1.06\,\mathrm{s}^{-1}$. The field is shown 10 buoyancy periods into the experiment, at which point the mixed

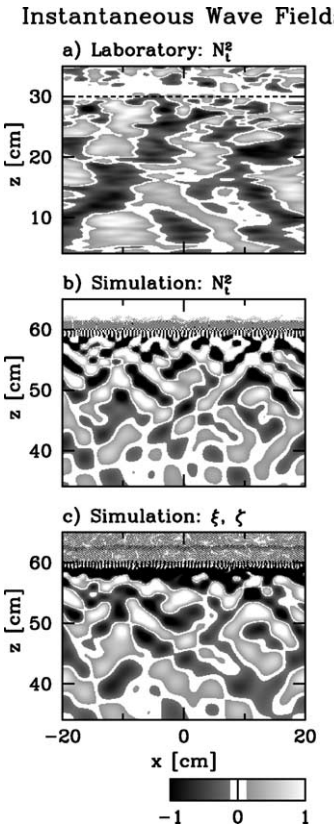

Fig. 4. Comparison of internal wave fields at time $= 10T_{\text{buoy}}$ for a laboratory experiment and a simulation. (a) The schlieren field, $\frac{\partial}{\partial t}\Delta N^2$, for a laboratory experiment. The mixed region is marked by the horizontal dashed line. (b) Schlieren field of a numerical simulation. The field of view corresponds to (a). (c) Vertical displacement field for the simulation in (b). The vorticity field is superimposed on the image. The aspect ratio of length to height is 1:1 in all figures. All fields are normalized and colour contours represent non-dimensional values. The colour map indicates regions of positive and negative fields.

region had deepened to $z = 30$ cm. The field shown, $N_t^2 \equiv \frac{\partial}{\partial t}\Delta N^2$, is the field directly measured by the synthetic schlieren technique and is the time derivative of the change to the background density. This field is sensitive to large local gradients to the background stratification, and due to the time derivative, filters out slower motions. Therefore, the schlieren field is more sensitive to the smaller-scale propagating waves than the modal waves. The displacement field can be directly related to the N_t^2 field for linear waves, so that the lines in the figure are parallel to the crests and troughs of the waves.

Numerical simulations are performed in which the spectral components of the vorticity field are forced at each time-step with white noise at the higher wavenumbers. The wavenumbers are continually forced with a Gaussian envelope centered at a peak wavenumber, k_f,

and with a spread of k_σ:

$$F^*_\zeta(k_x, k_z) = A^*_F \exp\left[-\frac{1}{2}\left(\frac{(k_x - k_f)^2 + (k_z - k_f)^2}{k_{\sigma^2}}\right)\right] \tag{9}$$

where * denotes the spectral component, A^*_F is a uniform random variable with $-F_0 \leq A^*_F \leq F_0$, and the amplitude of forcing $F_0 = 1000\,\mathrm{s}^{-2}$. The forcing wavenumber is $k_f = 13\,\mathrm{cm}^{-1}$ with a width in spectral space of $k_\sigma = 2\,\mathrm{cm}^{-1}$. This corresponds to forcing at scales centered around 0.5 cm.

In Fig. 4b is the schlieren field for a simulation in which $N = 1.0\,\mathrm{s}^{-1}$. The field of view shown has the same dimensions as in Fig. 4a, and is also at time $t = 10T_{\mathrm{buoy}}$. For clarity, the corresponding basic state fields of vertical displacement and vorticity are superimposed in the same frame of Fig. 4c in order to show the relative length scales in the two regions.

The wave field in the simulation shows many of the same properties as in the experiment. The angle of propagation of the waves in both figures is centered around $\Theta = 45^\circ$. As well, the length scales of the waves are in the intermediate range between the largest scales in the tank, $L = 40$ cm, and the forced scales in the mixed region, $L < 1$ mm. In particular, the scales of the N_i^2 field at the base of the mixed region ($z = 60$ cm) can be seen in Fig. 4b to be at least an order of magnitude smaller than the scales of the waves propagating down from the mixed region.

The dispersive nature of the wave field can be seen in both sets of images in that the scales of the wave field increase with distance from the mixed region.

Vertical time series of the schlieren fields for the experiment and the simulation in Fig. 4 are shown in Fig. 5. The time series are taken for 10 buoyancy periods, and begin when the oscillating grid is turned on and when the vorticity is first forced, respectively. In the experimental image, the large-scale waves appear as the chevron-shaped structures in the background. One advantage to the numerical simulation is the ability to separate the large-scale forcing from the small-scale turbulent forcing.

The regular structure to the wave field is the most noticeable feature of both of these time series. The same frequencies and the same length scales are present in both figures, despite the very different forcings to the mixed region, and despite the two-dimensionality of the simulations.

More pronounced in the simulation time series, although somewhat apparent in the experiment time series, is the appearance of a second region to the wave field after approximately $3T_{\mathrm{buoy}}$. The first, very regular, set of waves seems to be generated during the initial start-up of the simulations.

The frequencies present in the time series of Fig. 5b are shown in the power spectrum in Fig. 6. The power spectrum is calculated within the window $5T_{\mathrm{buoy}} \leq t \leq 15T_{\mathrm{buoy}}$ and $30 \leq z \leq 55$ cm, in order to be well within the wave field. The regularity in the time series is evident in the narrow range in spectral space, with the dominant peak corresponding to the angle of propagation $\Theta = 46 \pm 5^\circ$ calculated through the dispersion relation for linear internal waves:

$$\omega = N \cos\Theta. \tag{10}$$

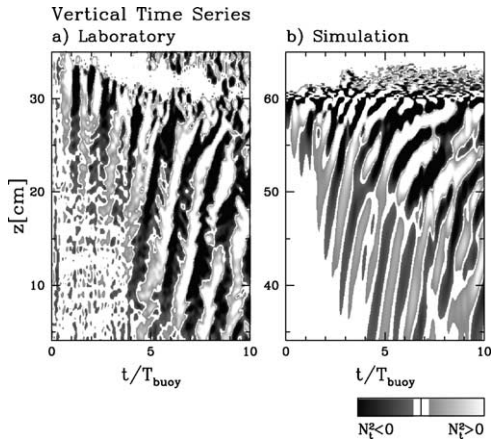

Fig. 5. Vertical time series of the N_t^2 fields corresponding to (a) the laboratory experiment in Fig. 4 and (b) the numerical simulation. In the experimental situation, the mixed region deepens from $z = 47$ cm to 35 cm within the the first 10 s, and then to $z = 30$ cm with the time frame of image.

In both simulations and laboratory experiments, the root-mean-square amplitudes of the waves calculated across a window within the developed region of the timeseries follow the same decrease with distance from the mixed region. Calculations of a linear wave field forced by the spectrum of waves at the base of the mixed region from the simulations has shown that this decrease in amplitude is not based solely on the dispersion of waves seen in the instantaneous fields in Fig. 4, and is likely due to diffusive effects.

Increasing the horizontal domain in the simulations results in the initial appearance of larger scales and larger amplitudes, and there seems to be a resonant phenomenon when the domain is doubled to $-40 \leq x \leq 40$ so that the tank-sized waves dominate the

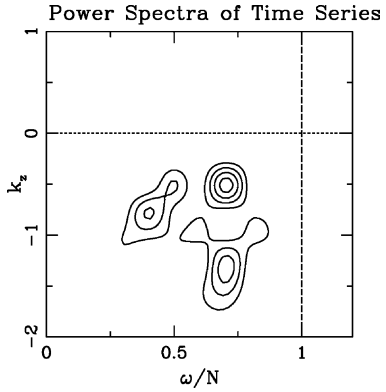

Fig. 6. Power spectrum of the time series for the numerical simulation in Fig 5(b). The largest peak corresponds to downward-propagating internal waves with angles of propagation of $\Theta = 46 \pm 5^\circ$. The maximum frequency for internal waves is marked by the vertical dashed line at $\omega = N$.

field and there is a shift in initial frequencies. When the domain is increased again to $-80 \leq x \leq 80$, larger amplitudes and initial horizontal scales appear. These do not dominate the field, although the amplitudes of the waves increase to the point of generating a significant wave-induced mean flow. The horizontal length scales seem to be affected by the width of the domain, but the vertical length scales are not set by the depth of the domain. For example, in Fig. 5, the vertical length scales are of the same order, although the numerical simulation is twice as deep as the experiment. As well, forcing the mixed region in a strip away from the base of the mixed region (as in the oscillating grid) $70 \leq z \leq 75$, also results in larger spatial scales. However, the angle of propagation of the waves after the initial generation remains centered on approximately 45° in all cases.

4. Discussion

The spectrum in Fig. 6 is typical of the spectra seen in the laboratory time series across the full range of experiments with different stratifications. The dominant laboratory wave frequencies calculated from the spectral peaks are shown in Fig. 7. The frequencies are plotted against the amplitudes of the waves as a fraction of their breaking amplitudes, A_{break}. The breaking amplitude is defined as the critical relative amplitude for wave breaking due to self-acceleration (Sutherland, 2001), where relative amplitude is defined by $A_{\text{rel}} = A_\xi/\lambda_x$, and A_ξ is the vertical displacement amplitude. The wave amplitudes are a significant fraction of their potential breaking amplitudes and their frequencies appear to be determined by the stratification.

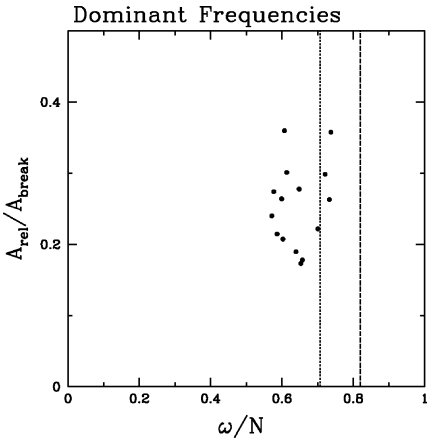

Fig. 7. The relative amplitudes, $A_{\text{rel}} = A_\xi/\lambda_x$, of the dominant laboratory waves, as a fraction of their breaking amplitudes, A_{break}, are plotted against their frequencies. The breaking amplitudes are defined as the critical relative amplitudes at which waves may break due to self-acceleration. The vertical dotted line marks the frequency at which $\Theta = 45°$, the dashed at which $\Theta = 35°$.

The vertical dotted line in Fig. 7 corresponds to an angle of propagation of $\Theta = 45^\circ$ and the dashed line corresponds to $\Theta = 35^\circ$. The former angle is of interest because for a fixed displacement amplitude, it is the angle at which waves carry the maximum vertical flux of horizontal momentum away from the turbulent region:

$$\rho_0 \langle u w \rangle = \frac{1}{4} \rho_0 N^2 A_\xi^2 \sin(2\Theta). \tag{11}$$

The vertical flux of energy carried by the waves is given by:

$$F_z = \frac{1}{2} \frac{\rho_0 A_\xi^2 N^3}{k_x} \sin\Theta \cos^2\Theta. \tag{12}$$

If the horizontal scale of the waves is fixed in addition to the amplitude, the maximum vertical flux of energy by the waves occurs for the maximum vertical group velocity, at $\Theta \approx 35^\circ$.

If the waves experience a significant decay within a short distance from the generation region, one would expect to observe the waves with the fastest vertical group

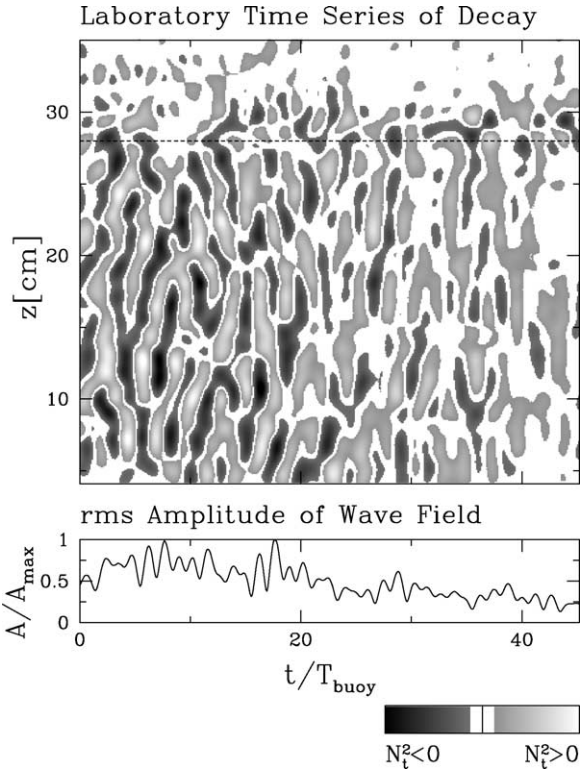

Fig. 8. Time series for the laboratory experiment in Fig. 5(a), started as the oscillating grid is turned off, to show the decay of the wave field in time. The mixed region extends to $z = 28$ cm. A plot of the root-mean-square amplitudes over the range $5 \le z \le 25$ cm is provided below, normalized by the maximum amplitude in the wave field.

velocity below the mixed region because these can travel the furthest before the effects of dissipation and diffusion reduce their amplitude. However, this explanation for our observations is unsatisfactory, as demonstrated by Fig. 8. This shows a continuation of the laboratory time series begun after the oscillating grid was stopped. At the bottom of the figure is a plot of the root-mean-square wave field in time averaged over $5 \leq z \leq 25$ cm. The waves decay slowly, and require 30 buoyancy periods in order to decay by 50 percent. Within 10 buoyancy periods, the wave field fills the tank, which suggests that the spectrum of the wave field in Fig. 6 would be much broader, and the dominant frequencies in Fig. 7 would lie closer to those corresponding to $\Theta = 35^\circ$.

Rather, the dominant wave propagation angle lies close to $\Theta = 45^\circ$, the angle at which waves would carry the most horizontal momentum away from the turbulent region. This suggests that there is an interaction between the wave field and the turbulent mixed region, which excites waves within a narrow frequency band. Further analysis of this hypothesis is the subject of ongoing research.

5. Conclusions

The numerical simulations in two-dimensions have the same qualitative results as the experiments with both the large-scale turbulent forcing and the small-scale turbulent forcing: large-scale, dominantly mode 2 waves are continuously generated by the mean circulation in the mixed region and random forcing across a range of scales excites downward-propagating waves with the same length-scales and frequencies as observed in experiments. This suggests that the most significant dynamics of the generation of waves from the mixed region is captured by the simulations.

The mixed region is kept turbulent in the laboratory experiments by an oscillating grid, which provides approximately horizontally homogeneous three-dimensional turbulence at scales less than the tank width. The simulations are in two-dimensions, and the mixed region is forced by white noise at high wavenumbers in the vorticity field. The comparisons between the laboratory experiments and the numerical simulations are encouraging, despite these differences.

The ratio of frequency to buoyancy frequency of the dominant downward-propagating waves consistently falls within a narrow band in both laboratory experiments and in numerical simulations under a variety of conditions. This narrow frequency range corresponds to waves with the maximum vertical transport of horizontal momentum, and appears to be a result of a wave-turbulence interaction.

Acknowledgements

This work has been supported by the Killam Trusts, the Natural Sciences and Engineering Research Council of Canada (NSERC), and the Canadian Foundation for Climate and Atmospheric Science (CFCAS).

References

Balmforth, N.J., Ierley, G.R., Young, W.R., 2002. Tidal conversion by subcritical topography. J. Phys. Ocean 32, 2900–2914.

Briggs, D.A., Ferziger, J.H., Koseff, J.R., Monismith, S.G., 1996. Entrainment in a shear-free turbulent mixing layer. J. Fluid Mech. 310, 215–241.

Dohan, K., Sutherland, B.R., 2002. Turbulence time-scales in mixing box experiments. Exp. Fluids 33, 709–719.

Dohan, K., Sutherland, B.R., 2003. Internal waves generated from a turbulent mixed region. Phys. Fluids 15, 488–498.

E, X., Hopfinger, X., 1986. On mixing across an interface in stably stratified fluid. J. Fluid Mech. 166, 227–244.

Egbert, G.D., Ray, R.D., 2000. Significant dissipation of tidal energy in the deep ocean inferred from satellite altimeter data. Nature 405, 775–778.

Fernando, H.J.S., Hunt, J.C.R., 1997. Turbulence, waves and mixing at shear-free density interfaces. Part 1. A theoretical model. J. Fluid Mech. 347, 197–234.

Ledwell, J.R., Montgomery, E.T., Polzin, K.L., Laurent, L.C.S., Schmitt, R.W., Toole, J.M., 2000. Evidence for enhanced mixing over rough topography in the abyssal ocean. Nature 403, 179–182.

Linden, P.F., 1975. The deepening of a mixed layer in a stratified fluid. J. Fluid Mech. 71, 385–405.

Llewellyn Smith, S.G., Young, W.R., 2002. Conversion of the barotropic tide. J. Phys. Ocean 32, 1554–1566.

McGrath, J.L., Fernando, H.J.S., Hunt, J.C.R., 1997. Turbulence, waves and mixing at shear-free density interfaces. Part 2. Laboratory experiments. J. Fluid Mech. 347, 235–261.

Munk, W., Wunsch, C., 1998. Abyssal recipes II: Energetics of tidal and wind mixing. Deep Sea Res. 45, 1977–2010.

Polzin, K.L., Toole, J.M., Ledwell, J.R., Schmitt, R.W., 1997. Spatial variability of turbulent mixing in the abyssal ocean. Science 276, 93–96.

St.Laurent, L., Garrett, C., 2002. The role of internal tides in mixing the deep ocean. J. Oceanogr. 58, 11–24.

Sutherland, B.R., 2001. Finite-amplitude internal wavepacket dispersion and breaking. J. Fluid Mech. 429, 343–380.

Sutherland, B.R., Dalziel, S.B., Hughes, G.O., Linden, P.F., 1999. Visualisation and measurement of internal waves by "synthetic schlieren". Part 1: Vertically oscillating cylinder. J. Fluid Mech. 390, 93–126.

Sutherland, B.R., Peltier, W.R., 1994. Turbulence transition and internal wave generation in density stratified jets. Phys. Fluids A 6, 1267–1284.

Trenberth, K.E., Caron, J.M., 2001. Estimates of meridional atmosphere and ocean heat transports. J. Climate 41, 3433–3443.